Commun. Comput. Phys.
doi: 10.4208/cicp.OA-2024-0220

Vol. **39**, No. 1, pp. 119-146
January 2026

An Efficient Time-Splitting Method to Simulate the Dynamics of Spin-Orbit Coupled Spin-1 Bose-Einstein Condensates

Xiaolan Chen[1], Yongjun Yuan[1,*] and Yong Zhang[2]

[1] *LCSM (MOE), School of Mathematics and Statistics, Hunan Normal University, Changsha, Hunan 410081, P.R. China.*

[2] *Center for Applied Mathematics and KL-AAGDM, Tianjin University, Tianjin, 300072, P.R. China.*

Received 24 September 2024; Accepted (in revised version) 20 May 2025

Abstract. In this paper, an efficient time-splitting Fourier spectral method is proposed to simulate the dynamics of spin-orbit coupled spin-1 Bose-Einstein condensates (SOC spin-1 BECs). We split the Hamiltonian into a linear part, which consists of the Laplace and SOC terms, and a nonlinear part that includes all the remaining terms. The linear subproblem is integrated analytically in phase space by solving an ordinary differential system of constant coefficient matrix. While, for the nonlinear subproblem, it is proved the coefficient matrix is actually time-independent in physical space, therefore, the nonlinear subproblem can be integrated exactly. Based on such two-step splitting, we construct high-order schemes to simulate the dynamics. Our method is spectrally accurate in space and high order in time. It is efficient, explicit, unconditionally stable and simple to implement. In addition, we derive some dynamical properties for SOC spin-1 BECs. Extensive numerical results are presented to confirm the accuracy and efficiency, illustrate the dynamical properties at discrete level, and show interesting physics of SOC spin-1 BECs, such as the SOC effects and different wave patterns.

AMS subject classifications: 35Q41, 65M70, 81Q05, 81V45

Key words: spin-1 Bose Einstein condensate, spin-orbit coupled, Gross-Pitaevskii equation, dynamics, fast Fourier transform, time-splitting method.

1 Introduction

Since its experimental realizations in 1995 [1, 11], the Bose-Einstein condensate (BEC) has stimulated great excitement in the physical community and regains vast interests

*Corresponding author. *Email addresses:* cxlan909@163.com (X. Chen), yyj1983@hunnu.edu.cn (Y. Yuan), Zhang_Yong@tju.edu.cn (Y. Zhang)

in atomic and molecular physics as well as condensate matter physics. In particular, the spin-orbit coupling (SOC), which was found that plays a crucial role in Majorana fermions [27], spintronic devices [18], spin Hall effect [15] and topological insulators [14], has been successfully induced in recent experiments in a neutral atomic BECs by dressing two atomic spin states with a pair of lasers [20–22]. These experiments triggered a strong activity in the area of spin-orbit-coupled cold atoms and a number of exciting phenomena have been discovered. The spin-1 BECs with isotropic spin-orbit coupling and rotation have been also studied [19,31].

It is well known that, in the mean field regime, the spin-$\mathcal{F}$ ($\mathcal{F}\in\mathbb{N}$) BEC can be well described by a system of $2\mathcal{F}+1$ coupled Gross-Pitaevskii equations (GPEs) when the temperature T is much smaller than the critical temperature T_c. Thus the spin-orbit coupled spin-1 BEC can be described by the macroscopic complex-valued vector wave function $\Psi=\Psi(\mathbf{x},t)=(\psi_1(\mathbf{x},t),\psi_0(\mathbf{x},t),\psi_{-1}(\mathbf{x},t))^T$ satisfying the GPEs

$$\begin{aligned}
i\hbar\partial_t\psi_1(\mathbf{x},t)&=\left[-\frac{\hbar^2}{2m}\nabla^2+V+\beta_0\rho+\beta_1F_z\right]\psi_1+\frac{\beta_1}{\sqrt{2}}F_-\psi_0-\gamma\widetilde{L}_0\psi_0,\\
i\hbar\partial_t\psi_0(\mathbf{x},t)&=\left[-\frac{\hbar^2}{2m}+V+\beta_0\rho\right]\psi_0+\frac{\beta_1}{\sqrt{2}}[F_+\psi_1+F_-\psi_{-1}]-\gamma(\widetilde{L}_0\psi_{-1}+\widetilde{L}_1\psi_1),\\
i\hbar\partial_t\psi_{-1}(\mathbf{x},t)&=\left[-\frac{\hbar^2}{2m}\nabla^2+V+\beta_0\rho-\beta_1F_z\right]\psi_{-1}+\frac{\beta_1}{\sqrt{2}}F_+\psi_0-\gamma\widetilde{L}_1\psi_0,\\
\psi_\ell(\mathbf{x},0)&=\psi_\ell^0(\mathbf{x}),\quad \ell=1,0,-1,
\end{aligned}\tag{1.1}$$

where $\mathbf{x}=(x,y,z)^\top\in\mathbb{R}^3$ is the Cartesian coordinate vector, t is time, $\hbar$ is the Planck constant, m is the atomic mass. $\beta_0=\frac{4\pi\hbar^2}{3m}(a_0+2a_2)$ and $\beta_1=\frac{4\pi\hbar^2}{3m}(a_2-a_0)$ are constants expressed in terms of the s-wave scattering lengths a_0 and a_2 for a scattering channel of total hyperfine spin 0 (antiparallel spin collision) and spin 2 (parallel spin collision), respectively. $\rho=\rho_1+\rho_0+\rho_{-1}$ is the total density with $\rho_\ell=|\psi_\ell|^2$ ($\ell=1,0,-1$) being the density of each spin component. $\widetilde{L}_0=\hbar(i\partial_x+\partial_y)$ and $\widetilde{L}_1=\hbar(i\partial_x-\partial_y)$ are the spin-orbit coupling operators, γ is the spin-orbit coupling strength. $V(\mathbf{x})$ is a given real-valued external trapping potential determined by the type of system under investigation. In most BEC experiments, a harmonic potential is chosen to trap the condensates, i.e.,

$$V(\mathbf{x})=\frac{1}{2}\left(\omega_x^2x^2+\omega_y^2y^2+\omega_z^2z^2\right),\tag{1.2}$$

where ω_v ($v=x,y,z$) are dimensionless constants representing the trapping frequencies in v-direction. The wave function is normalized according to

$$\|\Psi\|^2:=\int_{\mathbb{R}^3}\sum_{\ell=-1}^{1}|\psi_\ell(\mathbf{x},t)|^2\mathrm{d}\mathbf{x}=N,$$

where N is the total number of particles in the condensate. The spin vector $F=[F_x,F_y,F_z]^\top=[\Psi^{\mathsf{H}}f_x\Psi,\Psi^{\mathsf{H}}f_y\Psi,\Psi^{\mathsf{H}}f_z\Psi]^\top$, where Ψ^{H} is the conjugate transpose of Ψ and

$$f_x=\frac{1}{\sqrt{2}}\begin{pmatrix}0&1&0\\1&0&1\\0&1&0\end{pmatrix},\quad f_y=\frac{i}{\sqrt{2}}\begin{pmatrix}0&-1&0\\1&0&-1\\0&1&0\end{pmatrix},\quad f_z=\begin{pmatrix}1&0&0\\0&0&0\\0&0&-1\end{pmatrix}. \tag{1.3}$$

To be more detailed, we have

$$\begin{aligned}F_x&=\frac{1}{\sqrt{2}}[\bar{\psi}_1\psi_0+\bar{\psi}_0(\psi_1+\psi_{-1})+\bar{\psi}_{-1}\psi_0],\\F_y&=\frac{i}{\sqrt{2}}[-\bar{\psi}_1\psi_0+\bar{\psi}_0(\psi_1-\psi_{-1})+\bar{\psi}_{-1}\psi_0],\\F_z&=|\psi_1|^2-|\psi_{-1}|^2,\end{aligned}$$

with $\bar{f}$ the conjugate of function f and $F_\pm=F_x\pm iF_y$.

By introducing $t\to t/\omega_m$ with $\omega_m=\min\{\omega_x,\omega_y,\omega_z\}$, $\mathbf{x}\to\mathbf{x}a_s$ with $a_s=\sqrt{\hbar/(m\omega_m)}$, $\psi_\ell\to\sqrt{N}\psi_\ell/a_s^{3/2}$ ($\ell=1,0,-1$), and applying the dimension reduction strategy for a disk-shaped condensation (i.e., $\omega_x\approx\omega_y$ and $\omega_z\gg\omega_x$) [9], the d-dimensional (d=2 or d=3) dimensionless GPEs of (1.1) reads as

$$\begin{aligned}i\partial_t\psi_1(\mathbf{x},t)&=\left[-\frac{1}{2}\nabla^2+V+c_0\rho+c_1F_z\right]\psi_1+\frac{c_1}{\sqrt{2}}F_-\psi_0-\gamma L_0\psi_0,\\i\partial_t\psi_0(\mathbf{x},t)&=\left[-\frac{1}{2}\nabla^2+V+c_0\rho\right]\psi_0+\frac{c_1}{\sqrt{2}}[F_+\psi_1+F_-\psi_{-1}]-\gamma(L_0\psi_{-1}+L_1\psi_1),\\i\partial_t\psi_{-1}(\mathbf{x},t)&=\left[-\frac{1}{2}\nabla^2+V+c_0\rho-c_1F_z\right]\psi_{-1}+\frac{c_1}{\sqrt{2}}F_+\psi_0-\gamma L_1\psi_0,\\\psi_\ell(\mathbf{x},0)&=\psi_\ell^0(\mathbf{x}),\quad \mathbf{x}\in\mathbb{R}^d,\quad \ell=1,0,-1,\end{aligned} \tag{1.4}$$

where $c_0=\frac{N\beta_0}{a_s^3\hbar\omega_m}=\frac{4\pi N(a_0+2a_2)}{3a_s}$, $c_1=\frac{N\beta_1}{a_s^3\hbar\omega_m}=\frac{4\pi N(a_2-a_0)}{3a_s}$, $L_0=i\partial_x+\partial_y$, $L_1=i\partial_x-\partial_y$, and

$$V(\mathbf{x})=\frac{1}{2}\begin{cases}\gamma_x^2x^2+\gamma_y^2y^2, & d=2,\\ \gamma_x^2x^2+\gamma_y^2y^2+\gamma_z^2z^2, & d=3,\end{cases} \tag{1.5}$$

with $\gamma_\nu=\frac{\omega_\nu}{\omega_m}$ ($\nu=x,y,z$).

Note that the CGPEs (1.4) can be written in the following compact form

$$i\partial_t\Psi=\mathcal{H}\Psi:=\left[\left(-\frac{1}{2}\Delta+V+c_0\rho\right)I_3+c_1F\cdot f\ -\gamma\mathcal{S}\right]\Psi, \tag{1.6}$$

where $\mathcal{H}$ is the Hamiltonian with I_3 the 3×3 identity matrix and

$$F\cdot f=\begin{pmatrix}F_z&\frac{1}{\sqrt{2}}F_-&0\\\frac{1}{\sqrt{2}}F_+&0&\frac{1}{\sqrt{2}}F_-\\0&\frac{1}{\sqrt{2}}F_+&-F_z\end{pmatrix},\quad \mathcal{S}=\begin{pmatrix}0&L_0&0\\L_1&0&L_0\\0&L_1&0\end{pmatrix}.$$

There have been extensive mathematical and numerical studies on single component BECs. Most of them are concerned about the existence and computations of ground states as well as the properties of dynamics [4,6–8]. For the spinor BECs without SOC, the popular normalized gradient flow method [3, 10] and the time-splitting method [9, 25, 26] have been successfully applied to simulate the ground states and dynamics, respectively. In particular, efficient compact two-step time-splitting methods have been developed to simulate the dynamics of single component BECs [4, 5], spin-1 BECs [23] and spin-2 BECs [24] without SOC. Meanwhile, Gawryluk et al. proposed a unified two-step split operator method (SOM) [13] for computing dynamics of spinor BECs without and with dipolar interactions, and of degenerate Fermi gases. These methods take the Laplace and the remaining parts of the Hamiltonian as the first and second splitting operators, respectively. For the spinor BECs with SOC, a project gradient flow method was proposed to compute the ground states of the SOC spin-1 BEC [29]. And, a first-order standard Lie time-splitting Fourier spectral method, which is composed of four subproblems at each time step, was developed to simulate both the dynamics of SOC spin-1 BECs [16] and SOC spin-2 BECs [2].

It is worthwhile to point out that the proper way of splitting is interesting and important in terms of accuracy and efficiency. In this paper, we aim to carry out a comprehensive investigation of an efficient numerical method to simulate the dynamics of the SOC spin-1 BEC. Numerically, the most challenges lie in how to split the Hamiltonian into proper parts and solve the corresponding subproblems accurately and efficiently. In particular, if the Hamiltonian can be split into two parts with each corresponding subproblem being solved exactly and efficiently, it will be very convenient to construct high-order schemes for the CGPEs (1.4), thus reduce the computational costs to a great extent. To this end, we propose a high-order time-splitting Fourier spectral method to solve CGPEs (1.4). Actually, inspired by the splitting strategy proposed for the spin-1 BECs without SOC [23], we group the Laplace and SOC terms together as the linear part and denote it by $\mathcal{A}$ as follows

$$\mathcal{A}=\Big(-\frac{1}{2}\Delta\Big)I_3-\gamma\mathcal{S},$$

and leave the remaining part of the Hamiltonian as the nonlinear part, denoted by $\mathcal{B}$, as follows

$$\mathcal{B}=(V+c_0\rho)I_3+c_1F\cdot f.$$

In this way, the corresponding subproblem can be efficiently and exactly solved in either Fourier or physical space, regardless of the potential $V(\mathbf{x})$. Our method is spectrally accurate in space and high order in time. It is efficient, explicit, unconditionally stable and simple to implement. Meanwhile, the total computational cost is $CN_{tot}\log(N_{tot})$ with N_{tot} being the total grid number.

The rest of the paper is organized as follows. In Section 2, some dynamical properties of the spin-orbit coupled spin-1 BEC are demonstrated. In Section 3, we propose the efficient and exact time-splitting Fourier spectral method to numerically solve the CGPEs

(1.4), and based on this, construct high order schemes to simulate the dynamics of SOC spin-1 BECs. In Section 4, extensive numerical results are presented to investigate the convergence order, efficiency and to demonstrate the dynamical properties of SOC spin-1 BECs. Finally, conclusions are drawn in Section 5.

2 Dynamical properties

In this section, we demonstrate dynamical laws of mass, energy, magnetization and condensate width of the SOC spin-1 BEC (1.4). These dynamical laws are briefly presented and can be used as benchmarks for testing our numerical methods. From here after, we denote $\Re(f)$ the real part of the function f in this paper.

Mass and energy. Define the mass and energy of the spin-orbit coupled spin-1 BEC (1.4) as

$$\mathcal{N}(t)=\mathcal{N}(\Psi(\cdot,t)):=\int_{\mathbb{R}^d}\sum_{\ell=-1}^{1}|\psi_\ell|^2\mathrm{d}\mathbf{x}, \tag{2.1}$$

and

$$\begin{aligned}\mathcal{E}(t):=\mathcal{E}(\Psi(\cdot,t))=\int_{\mathbb{R}^d}\Bigg[&\sum_{\ell=-1}^{1}\left(\frac{1}{2}|\nabla\psi_\ell|^2+V(\mathbf{x})|\psi_\ell|^2\right)+\frac{c_0}{2}\rho^2\\&+\frac{c_1}{2}\left(|F_+|^2+|F_z|^2\right)-\gamma\left(L_0\psi_0\bar{\psi}_1+L_0\psi_{-1}\bar{\psi}_0+L_1\psi_1\bar{\psi}_0+L_1\psi_0\bar{\psi}_{-1}\right)\Bigg]\,\mathrm{d}\mathbf{x}.\end{aligned} \tag{2.2}$$

It is easy to check that the SOC spin-1 BEC (1.4) has two important invariants [16]: the mass (or normalization) of the wave function and the energy per particle, i.e.,

$$\mathcal{N}(\Psi(\cdot,t))=\mathcal{N}(\Psi(\cdot,0))=1,\qquad \mathcal{E}(\Psi(\cdot,t))=\mathcal{E}(\Psi(\cdot,0)). \tag{2.3}$$

Magnetization. The magnetization of the spin-orbit coupled spin-1 BEC (1.4) reads as

$$\begin{aligned}\mathcal{M}=\mathcal{M}(\Psi(\cdot,t))&:=\sum_{\ell=-1}^{1}\int_{\mathbb{R}^d}\ell|\psi_\ell(\mathbf{x},t)|^2\mathrm{d}\mathbf{x}\\&=\int_{\mathbb{R}^d}\left[|\psi_1(\mathbf{x},t)|^2-|\psi_{-1}(\mathbf{x},t)|^2\right]\mathrm{d}\mathbf{x}.\end{aligned} \tag{2.4}$$

By direct calculations, we obtain

$$\begin{aligned}\frac{d\mathcal{M}(t)}{dt}&=\frac{d}{dt}\int_{\mathbb{R}^d}\left[|\psi_1(\mathbf{x},t)|^2-\psi_{-1}(\mathbf{x},t)|^2\right]\mathrm{d}\mathbf{x}\\&=2\gamma\Re\int_{\mathbb{R}^d}\left[\bar{\psi}_{-1}(\partial_x+i\partial_y)\psi_0-\psi_1(\partial_x+i\partial_y)\bar{\psi}_0\right]\mathrm{d}\mathbf{x}.\end{aligned} \tag{2.5}$$

Thus the magnetization is conserved (i.e., $\mathcal{M}(t)=\mathcal{M}(0)$) for $\gamma=0$, while this conservation cannot be guaranteed if $\gamma\neq0$.

Condensate width. The condensate width of BEC at the direction of α is $\sigma_\alpha=\sqrt{\delta_\alpha(t)}$ ($t>0$, $\alpha=x,y$ or $r=\sqrt{x^2+y^2}$) is defined by

$$\delta_\alpha(t)=\sum_{\ell=-1}^{1}\delta_{\alpha,\ell}(t) \tag{2.6}$$

with

$$\delta_{\alpha,\ell}(t)=\int_{\mathbb{R}^d}\alpha^2|\psi_\ell(\mathbf{x},t)|^2\mathrm{d}\mathbf{x}. \tag{2.7}$$

In particular, when $d=2$, we have the following lemma for its dynamics.

Lemma 2.1. *Suppose $\Psi(\mathbf{x},t)$ be the solution of the* (1.4) *with the radially symmetric harmonic trap* (1.2)*, i.e., $\gamma_x=\gamma_y:=\gamma_r$, it holds*

$$\begin{aligned}\frac{d^2\delta_r(t)}{dt^2}=&\frac{d^2\delta_x(t)}{dt^2}+\frac{d^2\delta_y(t)}{dt^2}\\ =&-4\gamma_r^2\delta_r^2(t)+4\mathcal{E}\left(\Psi(\cdot,0)\right)+G(\gamma,\Psi(\cdot,t))\end{aligned} \tag{2.8}$$

with

$$\begin{aligned}G(\gamma,\Psi)=&4\gamma^2\Re\int_{\mathbb{R}^d}\Big[2|\psi_0|^2+|\psi_1|^2+|\psi_{-1}|^2\\ &+ix\left(\psi_1\partial_y\bar{\psi}_1-\psi_{-1}\partial_y\bar{\psi}_{-1}\right)-iy\left(\psi_1\partial_x\bar{\psi}_1-\psi_{-1}\partial_x\bar{\psi}_{-1}\right)\Big]\mathrm{d}\mathbf{x},\end{aligned}$$

where $\delta_r(t):=\delta_x(t)+\delta_y(t)$, $\delta_r^{(0)}=\delta_x(0)+\delta_y(0)$ and $\dot{\delta}_r^{(1)}=\dot{\delta}_x(0)+\dot{\delta}_y(0)$. Furthermore, if $d=2$, $\gamma=0$ and the initial data $\Psi^0(\mathbf{x})$ is radially symmetric, we have for $t\geq 0$,

$$\delta_x(t)=\delta_y(t)=\frac{1}{2}\delta_r(t)=\frac{\mathcal{E}(0)}{2\gamma_r^2}\left[1-\cos(2\gamma_r t)\right]+\delta_r^{(0)}\cos(2\gamma_r t)+\frac{\delta_r^{(1)}}{2\gamma_r}\sin(2\gamma_r t). \tag{2.9}$$

Thus, in this case the condensate widths $\sigma_x(t)$ and $\sigma_y(t)$ are periodic functions with frequency doubling trapping frequency.

Proof. Noticing (2.6)-(2.7) and taking (1.4) into account, we have

$$\begin{aligned}\frac{d\delta_{\alpha,1}(t)}{dt}=&\int_{\mathbb{R}^d}\alpha^2\left(\partial_t\psi_1\bar{\psi}_1+\psi_1\partial_t\bar{\psi}_1\right)\mathrm{d}\mathbf{x}\\ =&-i\int_{\mathbb{R}^d}\left[\alpha^2(i\partial_t\psi_1)\bar{\psi}_1-\alpha^2(-i\partial_t\bar{\psi}_1)\psi_1\right]\mathrm{d}\mathbf{x}\\ =&\int_{\mathbb{R}^d}\Big[i\alpha(\psi_1\partial_\alpha\bar{\psi}_1-\bar{\psi}_1\partial_\alpha\psi_1)+ic_1\alpha^2(\bar{\psi}_0^2\psi_1\psi_{-1}-\psi_0^2\bar{\psi}_1\bar{\psi_{-1}})\\ &-\gamma\alpha^2\psi_1(\partial_x+i\partial_y)\bar{\psi}_0-\gamma\alpha^2\bar{\psi}_1(\partial_x-i\partial_y)\psi_0\Big]\mathrm{d}\mathbf{x}.\end{aligned} \tag{2.10}$$

Similarly, we obtain

$$\begin{aligned}\frac{d\delta_{\alpha,0}(t)}{dt}=&\int_{\mathbb{R}^d}\Big[i\alpha(\psi_0\partial_\alpha\bar{\psi}_0-\bar{\psi}_0\partial_\alpha\psi_0)+2ic_1\alpha^2(\psi_0^2\bar{\psi}_1\bar{\psi_{-1}}-\bar{\psi}_0^2\psi_1\psi_{-1})\\&-\gamma\alpha^2\psi_0(\partial_x-i\partial_y)\bar{\psi}_1-\gamma\alpha^2\bar{\psi}_0(\partial_x+i\partial_y)\bar{\psi}_{-1}\\&-\gamma\alpha^2\bar{\psi}_0(\partial_x+i\partial_y)\psi_1-\gamma\alpha^2\bar{\psi}_0(\partial_x-i\partial_y)\psi_{-1}\Big]\mathrm{d}\mathbf{x},\end{aligned}\tag{2.11}$$

$$\begin{aligned}\frac{d\delta_{\alpha,-1}(t)}{dt}=&\int_{\mathbb{R}^d}\Big[i\alpha(\psi_{-1}\partial_\alpha\bar{\psi}_{-1}-\bar{\psi}_{-1}\partial_\alpha\psi_{-1})+ic_1\alpha^2(\bar{\psi}_0^2\psi_1\psi_{-1}-\psi_0^2\bar{\psi}_1\bar{\psi_{-1}})\\&-\gamma\alpha^2\psi_{-1}(\partial_x+i\partial_y)\bar{\psi}_0-\gamma\alpha^2\bar{\psi}_{-1}(\partial_x-i\partial_y)\psi_0\Big]\mathrm{d}\mathbf{x}.\end{aligned}\tag{2.12}$$

Combining (2.10)-(2.12), one obtains

$$\begin{aligned}\frac{d\delta_\alpha(t)}{dt}=&\int_{\mathbb{R}^d}\Big[\sum_{j=-1}^{1}i\alpha(\psi_j\partial_\alpha\bar{\psi}_j-\bar{\psi}_j\partial_\alpha\psi_j)\\&+2\gamma\alpha\Big(\psi_1\bar{\psi}_0(\partial_x+i\partial_y)\alpha+\psi_0\bar{\psi}_1(\partial_x-i\partial_y)\alpha\\&+\psi_0\bar{\psi}_{-1}(\partial_x+i\partial_y)\alpha+\bar{\psi}_0\psi_{-1}(\partial_x-i\partial_y)\alpha\Big)\Big]\mathrm{d}\mathbf{x},\end{aligned}\tag{2.13}$$

$$\begin{aligned}\frac{d^2\delta_\alpha(t)}{dt^2}=&\int_{\mathbb{R}^d}\Big[\frac{d}{dt}\Big(i\alpha(\psi_1\partial_\alpha\bar{\psi}_1-\bar{\psi}_1\partial_\alpha\psi_1)\Big)\\&+\frac{d}{dt}\Big(i\alpha(\psi_0\partial_\alpha\bar{\psi}_0-\bar{\psi}_0\partial_\alpha\psi_0)\Big)\\&+\frac{d}{dt}\Big(i\alpha(\psi_{-1}\partial_\alpha\bar{\psi}_{-1}-\bar{\psi}_{-1}\partial_\alpha\psi_{-1})\Big)\\&+\frac{d}{dt}\Big(2\gamma\alpha\big(\psi_1\bar{\psi}_0(\partial_x+i\partial_y)\alpha+\psi_0\bar{\psi}_1(\partial_x-i\partial_y)\alpha\\&\qquad+\psi_0\bar{\psi}_{-1}(\partial_x+i\partial_y)\alpha+\bar{\psi}_0\psi_{-1}(\partial_x-i\partial_y)\alpha\big)\Big)\Big]\mathrm{d}\mathbf{x}\\=&I+II+III+IV.\end{aligned}\tag{2.14}$$

Differentiating the above equation with respect to t, plugging (1.4) into each parts of

(2.14) and applying the integration by parts, we obtain

$$\begin{aligned}
I:=&\int_{\mathbb{R}^d}\Big[i\alpha(\partial_t\psi_1\partial_\alpha\bar{\psi}_1+\psi_1\partial_{\alpha t}\bar{\psi}_1-\partial_t\bar{\psi}_1\partial_\alpha\psi_1-\bar{\psi}_1\partial_{\alpha t}\psi_1)\Big]\mathrm{d}\mathbf{x}\\
=&\int_{\mathbb{R}^d}\Big[2\alpha\Big((i\partial_t\psi_1)\partial_\alpha\bar{\psi}_1+(-i\partial_t\bar{\psi}_1)\partial_\alpha\psi_1\Big)+\Big(\bar{\psi}_1(i\partial_t\psi_1)+\psi_1(-i\partial_t\bar{\psi}_1)\Big)\Big]\mathrm{d}\mathbf{x}\\
=&-2\gamma_r^2\delta_{\alpha,1}(t)+\int_{\mathbb{R}^d}\Big[2|\partial_\alpha\psi_1|^2-2c_0\alpha|\psi_1|^2\partial_\alpha\rho-2c_1\alpha|\psi_1|^2\partial_\alpha F_z\\
&-\sqrt{2}c_1\Re(F_-\psi_0\bar{\psi}_1)-2\sqrt{2}c_1\alpha\Re(\bar{\psi}_1\psi_0\partial_\alpha F_-+F_-\bar{\psi}_1\partial_\alpha\psi_0)\\
&-2\gamma\Re\big((L_0\psi_0)\bar{\psi}_1\big)-4\gamma\alpha\Re((L_0\psi_0)\partial_\alpha\bar{\psi}_1)\Big]\mathrm{d}\mathbf{x},
\end{aligned}\tag{2.15}$$

$$\begin{aligned}
II:=&-2\gamma_r^2\delta_{\alpha,0}(t)+\int_{\mathbb{R}^d}\Big[2|\partial_\alpha\psi_0|^2-2c_0\alpha|\psi_0|^2\partial_\alpha\rho\\
&+2\sqrt{2}c_1\alpha\Re(F_+\psi_1\partial_\alpha\bar{\psi}_0+F_-\psi_{-1}\partial_\alpha\bar{\psi}_0)+c_1|F_{+1}|^2\\
&-2\gamma\Re((L_0\psi_{-1})\bar{\psi}_0+(L_1\psi_1)\bar{\psi}_0)-4\gamma\alpha\Re\Big(\overline{(L_0\psi_{-1}+L_1\psi_1)}\partial_\alpha\psi_0\Big)\Big]\mathrm{d}\mathbf{x},
\end{aligned}\tag{2.16}$$

$$\begin{aligned}
III:=&-2\gamma_r^2\delta_{\alpha,-1}(t)+\int_{\mathbb{R}^d}\Big[2|\partial_\alpha\psi_{-1}|^2-2c_0\alpha|\psi_{-1}|^2\partial_\alpha\rho+2c_1\alpha|\psi_{-1}|^2\partial_\alpha F_z\\
&-\sqrt{2}c_1\Re(F_+\psi_0\bar{\psi}_{-1})-2\sqrt{2}c_1\alpha\Re(\bar{\psi}_{-1}\psi_0\partial_\alpha F_++F_+\bar{\psi}_{-1}\partial_\alpha\psi_0)\\
&-2\gamma\Re\big((L_1\psi_0)\bar{\psi}_{-1}\big)-4\gamma\alpha\Re\big((L_1\psi_0)\partial_\alpha\bar{\psi}_{-1}\big)\Big]\mathrm{d}\mathbf{x},
\end{aligned}\tag{2.17}$$

$$\begin{aligned}
IV:=&\frac{d}{dt}\int_{\mathbb{R}^d}\Big[2\gamma\alpha\Big(\psi_1\bar{\psi}_0(\partial_x+i\partial_y)\alpha+\psi_0\bar{\psi}_1(\partial_x-i\partial_y)\alpha\\
&+\psi_0\bar{\psi}_{-1}(\partial_x+i\partial_y)\alpha+\bar{\psi}_0\psi_{-1}(\partial_x-i\partial_y)\alpha\Big)\Big]\mathrm{d}\mathbf{x}\\
=&4\gamma\Re\int_{\mathbb{R}^d}(i\partial_x-\partial_y)\alpha\Big[(\psi_0\partial_\alpha\bar{\psi}_{-1}+\psi_1\partial_\alpha\bar{\psi}_0)\\
&+\gamma\Big(\alpha(L_0\psi_{-1})\bar{\psi}_{-1}+\alpha(L_0\bar{\psi}_1)\psi_1-(L_0\alpha)|\psi_0|^2-(L_1\alpha)\psi_1\bar{\psi}_{-1}\Big)\Big]\mathrm{d}\mathbf{x}.
\end{aligned}\tag{2.18}$$

Summing (2.15)-(2.18), we obtain

$$\begin{aligned}
\frac{d^2\delta_\alpha(t)}{dt^2}=&-2\gamma_r^2\delta_\alpha(t)+\int_{\mathbb{R}^d}\Big[2\sum_{j=-1}^{1}|\partial_\alpha\psi_j|^2+c_0\rho^2+c_1|F_z|^2+c_1|F_+|^2\\
&-2\gamma\Re\big((L_0\psi_0)\bar{\psi}_1\big)-2\gamma\Re((L_0\psi_{-1})\bar{\psi}_0+(L_1\psi_1)\bar{\psi}_0)-2\gamma\Re\big((L_1\psi_0)\bar{\psi}_{-1}\big)\\
&+G(\alpha,\gamma,\Psi)\Big]\mathrm{d}\mathbf{x},
\end{aligned}\tag{2.19}$$

with

$$\begin{aligned}G_1(\alpha,\gamma,\Psi)=&-4\gamma\alpha\Re\Big[(L_0\psi_0)\partial_\alpha\bar{\psi}_1+\overline{(L_0\psi_{-1}+L_1\psi_1)}\partial_\alpha\psi_0+(L_1\psi_0)\partial_\alpha\bar{\psi}_{-1}\Big]\\&+4\gamma\Re\Big[(i\partial_x-\partial_y)\alpha\Big((\psi_0\partial_\alpha\bar{\psi}_{-1}+\psi_1\partial_\alpha\bar{\psi}_0)\\&+\gamma\Big(\alpha(L_0\psi_{-1})\bar{\psi}_{-1}+\alpha(L_0\bar{\psi}_1)\psi_1-(L_0\alpha)|\psi_0|^2-(L_1\alpha)\psi_1\bar{\psi}_{-1}\Big)\Big)\Big].\end{aligned}$$

Hence, we have

$$\begin{aligned}\frac{d^2\delta_r(t)}{dt^2}=&\frac{d^2\delta_x(t)}{dt^2}+\frac{d^2\delta_y(t)}{dt^2}\\=&-4\gamma_r^2\delta_r(t)+\int_{\mathbb{R}^d}\Big[2\sum_{j=-1}^{1}\Big(|\nabla\psi_j|^2+V(\mathbf{x})|\psi_j|^2\Big)\\&+2c_0\rho^2+2c_1|F_z|^2+2c_1|F_+|^2-2\gamma\Re\big((L_0\psi_0)\bar{\psi}_1\big)\\&-2\gamma\Re\big((L_0\psi_{-1})\bar{\psi}_0+(L_1\psi_1)\bar{\psi}_0\big)-2\gamma\Re\big((L_1\psi_0)\bar{\psi}_{-1}\big)\\&+G_1(x,\gamma,\Psi)+G_1(y,\gamma,\Psi)\Big]\mathrm{d}\mathbf{x}\\=&-4\gamma_r^2\delta_r^2(t)+4E(\Psi(\cdot,0))+G(\gamma,\Psi(\cdot,t))\end{aligned}\tag{2.20}$$

with

$$\begin{aligned}G(\gamma,\Psi)=&G_1(x,\gamma,\Psi)+G_1(y,\gamma,\Psi)\\=&4\gamma^2\Re\int_{\mathbb{R}^d}\Big[\Big(2|\psi_0|^2+|\psi_1|^2+|\psi_{-1}|^2\\&+ix\big(\psi_1\partial_y\bar{\psi}_1-\psi_{-1}\partial_y\bar{\psi}_{-1}\big)-iy\big(\psi_1\partial_x\bar{\psi}_1-\psi_{-1}\partial_x\bar{\psi}_{-1}\big)\Big)\Big]\mathrm{d}\mathbf{x}.\end{aligned}$$

As a result, when $\gamma=0$, we have $G(0,\Psi)=0$. Thus the $\delta_r(t)$ given in (2.9) is the unique solution of the second order ODE (2.20) with the initial data $\delta_r(0)=\delta_r^{(0)}$ and $\dot{\delta}_r(0)=\dot{\delta}_r^{(1)}$.

Furthermore, if $\Psi^0(\mathbf{x})$ is radial symmetric, the solution $\Psi(\mathbf{x},t)$ is also radial symmetric since $\gamma_x=\gamma_y$, which implies that [4]

$$\delta_x(t)=\delta_y(t)=\frac{1}{2}\delta_r(t).$$

The proof is completed. □

3 Numerical method

In this section, we present a two step time-splitting method to solve the CGPEs (1.4) for studying the dynamics of SOC spin-1 BEC.

Due to the trapping potential, the wave function decays to zero exponentially fast at the far field. Thus in practical computation, we truncate the problem into a sufficiency large bounded computational domain $\mathcal{D}$ with periodic boundary conditions. To simplify the presentation, we will present the specific discrete scheme for the 2-dimensional (2D) case. Generalized to the 3-dimensional (3D) case is straightforward and the results remain valid without modifications. We choose the domain $\mathcal{D}:=[-L,L]^2$, the spatial mesh size $h=(2L)/N$ for N an even positive integer. The numerical results show that L should be chosen larger when the atom interaction parameter c_0, the SOC strength parameter γ and the evolution time T increase. Define the Fourier, physical index and grid points sets respectively as

$$\begin{aligned}
&\mathcal{I}_N=\left\{(j,k)\in\mathbb{Z}^2\,\middle|\, 0\le j\le N-1,\ 0\le k\le N-1\right\},\\
&\mathcal{T}_N=\left\{(p,q)\in\mathbb{Z}^2\,\middle|\, -\frac{N}{2}\le p\le \frac{N}{2}-1,\ -\frac{N}{2}\le q\le \frac{N}{2}-1\right\},\\
&\mathcal{G}=\left\{(x_j,y_k):=(-L+jh,-L+kh),\ \ (j,k)\in\mathcal{T}_N\right\}.
\end{aligned}$$

For a given time step $\tau>0$, we define the time sequence as $t_n=n\tau$ for $n=0,1,\cdots$. Let Ψ_{jk}^n be the numerical approximation of $\Psi(x_j,y_k,t_n)$ for $(j,k)\in\mathcal{I}_N, n>0$. The wave function is well approximated by Fourier spectral method. To be exact,

$$\phi_\ell(\mathbf{x})\approx\widetilde{\phi}_\ell(\mathbf{x}):=\sum_{(p,q)\in\mathcal{T}_N}\widehat{\phi}_{\ell,pq}\,e^{i\mu_p(x+L)}e^{i\mu_q(y+L)},\quad \ell=1,0,-1, \tag{3.1}$$

where $\mu_p=2\pi p/(2L)$, $\mu_q=2\pi q/(2L)$. The Fourier coefficients

$$\widehat{\phi}_{\ell,pq}=\frac{1}{(2L)^2}\int_{\mathcal{D}}\phi_\ell(\mathbf{x})e^{-i\mu_p(x+L)}e^{-i\mu_q(y+L)}\mathrm{d}\mathbf{x}$$

are well approximated by applying trapezoidal rule to the above integral as follows

$$\widehat{\phi}_{\ell,pq}\approx\frac{1}{N^2}\sum_{(j,k)\in\mathcal{I}_N}\phi_{\ell,jk}\,e^{-i\mu_p(x_j+L)}e^{-i\mu_q(y_k+L)},$$

which can be accelerated by the discrete Fast Fourier Transform (FFT) within $\mathcal{O}(N^2\log N^2)$ float operations. In the following, we shall focus on the numerical computation of the linear and nonlinear subproblem in details.

3.1 Exact integrator of the linear subproblem

The first step of the time-splitting method is to solve the linear subproblem

$$\begin{cases} i\partial_t\Psi(\mathbf{x},t)=\mathcal{A}\,\Psi(\mathbf{x},t), & t_n\le t\le t_{n+1},\\ \Psi(\mathbf{x},t_n)=\Psi^n, & \mathbf{x}\in\mathcal{D}, \end{cases} \tag{3.2}$$

where $\mathcal{A}$ is the Laplace-SOC operator given below

$$\mathcal{A}=\Big(-\frac{1}{2}\Delta\Big)I_3-\gamma\begin{pmatrix}0 & L_0 & 0\\ L_1 & 0 & L_0\\ 0 & L_1 & 0\end{pmatrix}.$$

Taking Fourier transform at both sides of (3.2), for any fixed Fourier mode $(p,q)\in\mathcal{T}_N$, we obtain the constant coefficient linear ODE system in the phase space below

$$i\partial_t\widehat{\Psi}_{pq}(t)=\begin{pmatrix}\frac{a}{2} & \gamma b & 0\\ \gamma c & \frac{a}{2} & \gamma b\\ 0 & \gamma c & \frac{a}{2}\end{pmatrix}\widehat{\Psi}_{pq}(t):=\hat{A}\widehat{\Psi}_{pq}(t),\quad t_n\le t\le t_{n+1},\tag{3.3}$$

where $\widehat{\Psi}_{pq}(t)=\big(\widehat{\psi}_{1,pq}(t),\widehat{\psi}_{0,pq}(t),\widehat{\psi}_{-1,pq}(t)\big)^\top$, $a=\mu_p^2+\mu_q^2$, $b=\mu_p-i\mu_q$ and $c=\mu_p+i\mu_q$. Obviously, the solution to (3.3) reads as

$$\widehat{\Psi}_{pq}(t)=e^{-i(t-t_n)\hat{A}}\widehat{\Psi}_{pq}(t_n):=W_{pq}(t)\ \widehat{\Psi}_{pq}(t_n),\quad t_n\le t\le t_{n+1}.\tag{3.4}$$

The matrix W_{pq} is reduced to identity matrix I_3 for $(p,q)=(0,0)$ since $a=b=c=0$. For nonzero Fourier modes, i.e., $(p,q)\neq(0,0)$, due to $\hat{A}$ is a Hermitian matrix, i.e., $(\hat{A})^{\mathsf{H}}=\hat{A}$, similar to the trick of diagonalizing the matrix [2,16,23], we can diagonalize $\hat{A}$ explicitly using a unitary matrix U (i.e., $UU^{\mathsf{H}}=U^{\mathsf{H}}U=I_3$) to a real diagonal matrix, such that $\hat{A}=U\Lambda U^{\mathsf{H}}$. That is,

$$U=\begin{pmatrix}\frac{b}{\sqrt{2a}} & \frac{b}{2\sqrt{a}} & \frac{b}{2\sqrt{a}}\\ 0 & -\frac{\sqrt{2}}{2} & \frac{\sqrt{2}}{2}\\ -\frac{c}{\sqrt{2a}} & \frac{c}{2\sqrt{a}} & \frac{c}{2\sqrt{a}}\end{pmatrix},\quad \Lambda=\begin{pmatrix}\lambda_1 & 0 & 0\\ 0 & \lambda_2 & 0\\ 0 & 0 & \lambda_3\end{pmatrix}$$

with $\lambda_1=\frac{a}{2}$, $\lambda_2=\frac{a}{2}-\gamma\sqrt{2a}$ and $\lambda_3=\frac{a}{2}+\gamma\sqrt{2a}$. Direct calculations yields

$$\begin{aligned}W_{pq}(t)=e^{-i(t-t_n)\hat{A}}&=U\begin{pmatrix}e^{-i\lambda_1(t-t_n)} & 0 & 0\\ 0 & e^{-i\lambda_2(t-t_n)} & 0\\ 0 & 0 & e^{-i\lambda_3(t-t_n)}\end{pmatrix}U^{\mathsf{H}}\\ &=e^{\frac{-ia(t-t_n)}{2}}\left[A_1+\cos\Big(\sqrt{2a}\gamma(t-t_n)\Big)A_2-\frac{i}{\sqrt{2a}}\sin\Big(\sqrt{2a}\gamma(t-t_n)\Big)A_3\right],\end{aligned}\tag{3.5}$$

with

$$A_1=\begin{pmatrix}\frac{1}{2} & 0 & -\frac{b}{2c}\\ 0 & 0 & 0\\ -\frac{c}{2b} & 0 & \frac{1}{2}\end{pmatrix},\quad A_2=\begin{pmatrix}\frac{1}{2} & 0 & \frac{b}{2c}\\ 0 & 1 & 0\\ \frac{c}{2b} & 0 & \frac{1}{2}\end{pmatrix},\quad A_3=\begin{pmatrix}0 & b & 0\\ c & 0 & b\\ 0 & c & 0\end{pmatrix}.$$

Now, the solution to the linear subproblem (3.2) can be obtained.

Lemma 3.1. *Assume $\Psi(\mathbf{x},t)$ is the solution of* (3.2)*, then it holds*

$$\Psi(\mathbf{x},t)=\sum_{(p,q)\in\mathcal{T}_N}\Big[W_{pq}(t)\widehat{\Psi}_{pq}(t_n)\Big]e^{i\mu_p(x+L)}e^{i\mu_q(y+L)},\quad t_n\le t\le t_{n+1},\tag{3.6}$$

where $W_{pq}(t)$ are given by (3.5)*.*

Proof. Taking (3.1) and (3.4)-(3.5) into account, Lemma 3.1 is proved. □

Then we consider the conservation property of total mass at the discrete level. Define the discrete l^2-norm of $\Psi^n(\mathbf{x})=\left(\psi_1^n(\mathbf{x}),\psi_0^n(\mathbf{x}),\psi_{-1}^n(\mathbf{x})\right)^T$ on the interval $\mathcal{D}=(-L,L)^2$ as

$$\|\Psi^n\|_{l^2}=\sqrt{\left(\frac{2L}{N}\right)^2\sum_{\ell=-1}^{1}\sum_{(j,k)\in\mathcal{I}_N}\left|\psi_{\ell,jk}^n\right|^2}, \tag{3.7}$$

with $\psi_{\ell,jk}^n$ the approximation of $\psi_\ell(x_j,y_k,t_n)$ $(\ell=1,0,-1)$.

Lemma 3.2. *The solution* (3.6) *to the fist subproblem of the time splitting method is unconditionally stable for the GPEs* (3.2) *in 2D space, that is,*

$$\|\Psi(t)\|_{l^2}=\|\Psi^n\|_{l^2},\quad \forall\, t\in[t_n,t_{n+1}].$$

Proof. According to (3.4), we have $\forall t\in[t_n,t_{n+1}]$, $\widehat{\Psi}_{pq}(t)=e^{-i(t-t_n)\hat{A}}\widehat{\Psi}_{pq}^n$ with $(\hat{A})^{\mathsf{H}}=\hat{A}$. Therefore

$$\left(\widehat{\Psi}_{pq}(t)\right)^{\mathsf{H}}\widehat{\Psi}_{pq}(t)=\left(\widehat{\Psi}_{pq}^n\right)^{\mathsf{H}}\widehat{\Psi}_{pq}^n,\quad t\in[t_n,t_{n+1}].$$

By using the identities

$$\sum_{(j,k)\in\mathcal{I}_N}e^{i2\pi(k_1-l_1)j/M}e^{i2\pi(k_2-l_2)k/N}=\begin{cases}0, & k_1-l_1\neq mM \quad\text{or}\quad k_2-l_2\neq nN,\\ MN, & k_1-l_1=mM \quad\&\quad k_2-l_2=nN,\end{cases} \tag{3.8}$$

and

$$\sum_{(p,q)\in\mathcal{T}_N}e^{i2\pi(k_1-l_1)p/M}e^{i2\pi(k_2-l_2)q/N}=\begin{cases}0, & k_1-l_1\neq mM \quad\text{or}\quad k_2-l_2\neq nN,\\ MN, & k_1-l_1=mM \quad\&\quad k_2-l_2=nN,\end{cases} \tag{3.9}$$

with m and n being integers, it yields

$$\begin{aligned}
&\frac{\|\Psi(t)\|_{l^2}^2}{(2L)^2}=\frac{1}{N^2}\sum_{\ell=-1}^{1}\sum_{(j,k)\in\mathcal{I}_N}\left|\psi_{\ell,jk}(t)\right|^2\\
&=\frac{1}{N^2}\sum_{\ell=-1}^{1}\sum_{(j,k)\in\mathcal{I}_N}\left|\sum_{(p,q)\in\mathcal{T}_N}e^{i\mu_p(x_j+L)}e^{i\mu_q(y_k+L)}\widehat{\psi}_{\ell,pq}(t)\right|^2=\sum_{\ell=-1}^{1}\sum_{(p,q)\in\mathcal{T}_N}\left|\widehat{\psi}_{\ell,pq}(t)\right|^2\\
&=\sum_{(p,q)\in\mathcal{T}_N}\left(\widehat{\Psi}_{pq}(t)\right)^{\mathsf{H}}\widehat{\Psi}_{pq}(t)=\sum_{(p,q)\in\mathcal{T}_N}\left(\widehat{\Psi}_{pq}^n\right)^{\mathsf{H}}\widehat{\Psi}_{pq}^n\\
&=\sum_{\ell=-1}^{1}\sum_{(p,q)\in\mathcal{T}_N}\left|\widehat{(\psi^n)}_{\ell,pq}\right|^2=\sum_{\ell=-1}^{1}\sum_{(p,q)\in\mathcal{T}_N}\left|\sum_{(j,k)\in\mathcal{I}_N}e^{-i\mu_p(x_j+L)}e^{-i\mu_q(y_k+L)}\psi_{\ell,jk}^n\right|^2\\
&=\frac{1}{N^2}\sum_{\ell=-1}^{1}\sum_{(j,k)\in\mathcal{I}_N}\left|\psi_{\ell,jk}^n\right|^2=\frac{\|\Psi^n\|_{l^2}^2}{(2L)^2},
\end{aligned} \tag{3.10}$$

which implies $\|\Psi(t)\|_{l^2}=\|\Psi^n\|_{l^2}$, $\forall\, t\in[t_n,t_{n+1}]$. □

3.2 Exact integrator of the nonlinear subproblem

The second step is to solve the nonlinear subproblem

$$\begin{cases} i\partial_t\Psi(\mathbf{x},t)=\mathcal{B}(\Psi)\,\Psi(\mathbf{x},t), & t_n\le t\le t_{n+1},\\ \Psi(\mathbf{x},t_n)=\Psi^n, & \mathbf{x}\in\mathcal{D}, \end{cases} \tag{3.11}$$

where

$$\mathcal{B}=(V+c_0\rho)I_3+c_1\begin{pmatrix} F_z & \frac{1}{\sqrt{2}}F_- & 0\\ \frac{1}{\sqrt{2}}F_+ & 0 & \frac{1}{\sqrt{2}}F_-\\ 0 & \frac{1}{\sqrt{2}}F_+ & -F_z \end{pmatrix}:=\mathcal{B}_1+c_1\mathcal{B}_2.$$

Fortunately, the coefficient matrix $\mathcal{B}$ is actually time independent, i.e., $\mathcal{B}(t)\equiv\mathcal{B}(t_n),\forall t\in[t_n,t_{n+1}]$. Noticing the facts that $f_\nu(\nu=x,y,z)$ and $\mathcal{B}$ are all Hermitian matrices, i.e.,

$$f_\nu^{\mathsf{H}}=f_\nu,\quad \mathcal{B}^{\mathsf{H}}=\mathcal{B},$$

and they satisfy the commutating relations $[f_x,f_y]:=f_xf_y-f_yf_x=if_z$, $[f_y,f_z]=if_x$ and $[f_z,f_x]=if_y$, we obtain the following lemma.

Lemma 3.3. *Assume $\Psi(\mathbf{x},t)$ is the solution to* (3.11)*, then the coefficient matrix $\mathcal{B}(\Psi)$* (3.11) *is independent of time t, that is*

$$\mathcal{B}(\Psi(t))\equiv\mathcal{B}(\Psi^n),\quad \mathcal{B}_2(\Psi(t))\equiv\mathcal{B}_2(\Psi^n),\quad \forall\, t_n\le t\le t_{n+1}.$$

Proof. It is sufficient to prove $\partial_t\rho=0$ and $\partial_tF_\nu=0$ $(\nu=x,y,z)$. We have

$$\partial_t\rho=\partial_t(\Psi^{\mathsf{H}}\Psi)=(\partial_t\Psi^{\mathsf{H}})\Psi+\Psi^{\mathsf{H}}\partial_t\Psi=i\left(\Psi^{\mathsf{H}}\mathcal{B}^{\mathsf{H}}\partial_t\Psi-\Psi^{\mathsf{H}}\mathcal{B}\partial_t\Psi\right)=0,$$

and

$$\begin{aligned}\partial_tF_\nu&=\partial_t(\Psi^{\mathsf{H}}f_\nu\Psi)=i\Psi^{\mathsf{H}}\mathcal{B}f_\nu\Psi-i\Psi^{\mathsf{H}}f_\nu\mathcal{B}\Psi\\&=ic_1\Psi^{\mathsf{H}}[\mathbf{F}\cdot\mathbf{f},f_\nu]\Psi=ic_1\Psi^{\mathsf{H}}[F_xf_x+F_yf_y+F_zf_z,f_\nu]\Psi\\&=ic_1\left(F_x\Psi^{\mathsf{H}}[f_x,f_\nu]\Psi+F_y\Psi^{\mathsf{H}}[f_y,f_\nu]\Psi+F_z\Psi^{\mathsf{H}}[f_z,f_\nu]\Psi\right)=0,\quad \nu=x,y,z.\end{aligned}$$

These imply that the total density $\rho(\Psi(t))\equiv\rho(\Psi^n)$, the spin vector $F_\nu(\Psi(t))\equiv F_\nu(\Psi^n)$ is conserved, $\mathcal{B}(\Psi(t))\equiv\mathcal{B}(\Psi^n)$ and $\mathcal{B}_2(\Psi(t))\equiv\mathcal{B}_2(\Psi^n)$, $\forall\, t_n\le t\le t_{n+1}$. □

It is clear that Eq. (3.11) becomes a linear ordinary differential system and the exact solution is given explicitly in the following lemma.

Lemma 3.4. *Assume that $\Psi(\mathbf{x},t)$ is the solution to subproblem* (3.11)*, then*

$$\Psi(\mathbf{x},t)=e^{-i(t-t_n)(V+c_0\rho^n)}\left[\cos(c_1(t-t_n)|F^n|)\Psi^n-\frac{i}{|F^n|}\sin(c_1(t-t_n)|F^n|)\mathcal{B}_2^n\Psi^n\right], \tag{3.12}$$

where matrix $\mathcal{B}_2^n:=\mathcal{B}_2(\Psi(t_n))$.

Proof. Obviously, the exact solution of (3.11) reads as follows

$$\Psi(\mathbf{x},t)=e^{-i(t-t_n)\mathcal{B}^n}\Psi^n=e^{-i(t-t_n)(V+c_0\rho^n)}e^{-ic_1(t-t_n)\mathcal{B}_2}\Psi^n. \tag{3.13}$$

One finds that the eigenvalues of $\mathcal{B}_2$ are $|F^n|,-|F^n|$ and 0. The associated eigenvectors are v_1^n, v_2^n and $v_3^n=|F^n|^{-1}2^{-\frac{1}{2}}(-F_-^n,\sqrt{2}F_z^n,F_+^n)^\top$. In fact, we can expand the wave function vector Ψ^n with respect to the above eigenvectors as $\Psi^n=\alpha_1v_1^n+\alpha_2v_2^n+\alpha_3v_3^n$. It is easy to prove that $\alpha_3=\langle\Psi^n,v_3^n\rangle=0$ by substituting the explicit formula of α_3^n as follows

$$\begin{aligned}\alpha_3&=\langle\Psi^n,v_3^n\rangle=|F^n|^{-1}(-\psi_1^nF_+^n/\sqrt{2}+\psi_0^nF_z^n+\psi_{-1}^nF_-^n/\sqrt{2})\\&=|F^n|^{-1}\big(-\psi_1^n(\bar{\psi}_1^n\psi_0^n+\bar{\psi}_0^n\psi_{-1}^n)+\psi_0^n(|\psi_1^n|^2-|\psi_{-1}^n|^2)+\psi_{-1}^n(\psi_1^n\bar{\psi}_0^n+\psi_0^n\bar{\psi}_{-1}^n)\big)\\&=0.\end{aligned}$$

Therefore, we have $\Psi^n=\alpha_1v_1^n+\alpha_2v_2^n$. Since $\mathcal{B}_2^{\mathsf{H}}=\mathcal{B}_2$, we obtain

$$\begin{aligned}e^{-ic_1(t-t_n)\mathcal{B}_2}\Psi^n&=(v_1^n,v_2^n,v_3^n)\begin{pmatrix}e^{-ic_1(t-t_n)|F^n|}&0&0\\0&e^{ic_1(t-t_n)|F^n|}&0\\0&0&0\end{pmatrix}\begin{pmatrix}(v_1^n)^{\mathsf{H}}\\(v_2^n)^{\mathsf{H}}\\(v_3^n)^{\mathsf{H}}\end{pmatrix}(\alpha_1v_1^n+\alpha_2v_2^n)\\&=\alpha_1e^{-ic_1(t-t_n)|F^n|}v_1^n+\alpha_2e^{ic_1(t-t_n)|F^n|}v_2^n\\&=\cos(c_1(t-t_n)|F^n|)\Psi^n-\frac{i}{|F^n|}\sin(c_1(t-t_n)|F^n|)\mathcal{B}_2^n\Psi^n.\end{aligned}$$

This completes the proof. □

Similarly, the solution to the nonlinear subproblem (3.11) preserves the conservation property of total mass on the discrete level.

Lemma 3.5. *Suppose $\Psi(\mathbf{x},t)$ is the solution to subproblem* (3.11)*, then*

$$\|\Psi(t)\|_{l^2}=\|\Psi^n\|_{l^2},\quad\forall\, t\in[t_n,t_{n+1}].$$

Proof. Since $\mathcal{B}^n$ is a Hermitian matrix, therefore, its eigenvalues are all real. Then we have

$$\|\Psi(t)\|_{l^2}^2=\|e^{-i(t-t_n)\mathcal{B}^n}\Psi^n\|_{l^2}^2=\|\Psi^n\|_{l^2}^2, \tag{3.14}$$

which completes the proof. □

We remark that, using Lemma 3.2 and Lemma 3.5, we can see that our time-splitting Fourier spectral method is unconditionally stable.

3.3 Algorithms for the time-splitting Fourier spectral method

In this subsection, we construct high-order time marching schemes to implement the time-splitting Fourier spectral method. Denote $\Psi(t)=e^{-i(t-t_n)\mathcal{A}}\Psi^n$ and $\Psi(t)=e^{-i(t-t_n)\mathcal{B}}\Psi^n$ the solutions of the subproblems (3.2) and (3.11), respectively. In principle, splitting approximations of higher order accuracy can be constructed as [28]

$$\Psi^{n+1}=\left(\prod_{j=1}^{m}e^{-ia_j\tau\mathcal{A}}e^{-ib_j\tau\mathcal{B}}\right)\Psi^n, \tag{3.15}$$

where the coefficients a_j and b_j $(j=1,\cdots,m)$ are chosen properly. The classical second-order Strang splitting [4, 6] is $m=2$, $a_1=a_2=1/2$, $b_1=1$, $b_2=0$. And, one of the most frequently used fourth-order symplectic time integrators is $m=4$, that is

$$\begin{aligned} &a_1=a_3=\frac{1}{2-2^{1/3}},\quad a_2=-\frac{2^{1/3}}{2-2^{1/3}},\quad a_4=0,\\ &b_1=b_4=\frac{1}{2(2-2^{1/3})},\quad b_2=b_3=\frac{1-2^{1/3}}{2(2-2^{1/3})}. \end{aligned} \tag{3.16}$$

In practice, from time $t=t_n$ to $t=t_{n+1}$, we combine the splitting steps via the standard Strang splitting and present detailed step-by-step algorithm proposed in Algorithm 1. The algorithm for the Yoshida fourth-order scheme [7, 12, 28] can be similarly proposed, here we skip it for brevity.

Algorithm 1 Second-order splitting Fourier spectral method

1: Solve ODEs (3.11) by (3.12) for half time step $\tau/2$ with initial data given at $t=t_n$.
2: Solve ODEs (3.2) by (3.6) for one step τ starting with the data obtained from step 1.
3: Solve ODEs (3.11) by (3.12) for half time step $\tau/2$ again with the initial data obtained from step 2.

Remark 3.1 (**Efficiency).** For each time step, by the adopt of FFT in spatial, the computation costs of the second-order Strang splitting and the fourth-order Yoshida splitting scheme are $8N_{tot}+3N_{tot}\log(N_{tot})$ and $16N_{tot}+6N_{tot}\log(N_{tot})$ respectively.

Remark 3.2 (**Arbitrary high-order schemes).** It is simple to construct arbitrary high-order schemes based on (3.15) since both subproblems can be exactly integrated.

We point out that the only time discretization error of above second- and fourth-order time-splitting scheme are the splitting errors, which are second and fourth order in τ for any fixed mesh size $h>0$, respectively. Also, the schemes are explicit and unconditionally stable.

4 Numerical experiment

In this section, we first test the accuracy and efficiency of our numerical method for computing the dynamics of SOC spin-1 BECs (1.4). Then, we study the dynamical properties, including the energy, mass, magnetization and condensate widths. Finally, we apply our method to investigate some interesting phenomena. All algorithms were implemented in Matlab (2022a) and run on a 1.60GH Intel(R) Core(TM) i5-8265U CPU with a 6 MB cache in Windows. From here after, we adopt the length, time, and energy units as $a_s=\sqrt{\hbar/(m\omega_m)}$, $t_s=1/\omega_m$, and $\hbar\omega_m$, respectively.

4.1 Accuracy and efficiency test

In this part, the numerical error is measured in following norm:

$$\varepsilon_m := \frac{\|\psi_m(t)-\psi_m^{(h,\tau)}\|_{l^2}}{\|\psi_m(t)\|_{l^2}}, \quad m=1,0,-1, \tag{4.1}$$

where $\psi_m^{(h,\tau)}(t)$ is the numerical solution at time t obtained with mesh size h and time step τ, $\psi_m(t)$ is the "exact" solution. Hereafter, we denote the second-order time-splitting Fourier spectral method based on the Strang splitting as **TS2**, and the fourth-order time splitting method based on the Yoshida scheme as **TS4**.

To investigate the convergence, let $\psi_m(t)$ represents the numerical solution by the **TS4** with very fine mesh size $h=1/64$ and small time step $\tau=10^{-4}$, and assume it to be a sufficiently good representation of the exact solution at time t. Meanwhile, the efficiency performance of our **TS2** and **TS4** can be tested by investigating the computational costs, in terms of computational time, as a function of the total grid number.

Example 4.1. In order to show the accuracy of **TS2** and **TS4**, set $d=2$, $\mathcal{D}=[-8,8]^2$, $V(\mathbf{x})=\frac{1}{2}(x^2+y^2)$, $c_0=100$, $c_1=-2$, $\gamma=0.5$. Choose $\Phi^0(\mathbf{x})$ with $\|\Phi^0\|_{l^2}=1$, e.g.,

$$\psi_1^0=\frac{0.3343}{\sqrt{\pi}}\phi(\mathbf{x}), \quad \psi_0^0=\frac{0.8812}{\sqrt{\pi}}\phi(\mathbf{x}), \quad \psi_{-1}^0=\frac{0.3343}{\sqrt{\pi}}\phi(\mathbf{x}), \tag{4.2}$$

with $\phi(\mathbf{x})=e^{-(x^2+y^2)/2}$. Then compute the numerical errors by **TS2** and **TS4**, respectively, for

- **Case i**: $\tau=10^{-4}$ and $h=1/2,1/4,1/8,1/16$.
- **Case ii**: $h=1/64$ and $\tau=1/40,1/80,1/160,1/320,1/640$.

Tables 1-2 list the spatial errors and temporal errors of Example 4.1 at time $t=0.4$ for the 2D CGPE, from which we can conclude that **TS2/TS4** is second/fourth order accurate in time and spectrally accurate in space. A higher order operator splitting scheme is possible because both subproblems can be integrated exactly.

Table 1: Spatial discretization errors at time $t=0.4$ in Example 4.1.

h	1/2	1/4	1/8	1/16
		TS2		
$\mathcal{E}_1$	2.14E-01	3.95E-03	4.23E-08	7.91E-10
$\mathcal{E}_0$	1.53E-01	2.94E-03	2.90E-08	4.84E-10
$\mathcal{E}_{-1}$	2.10E-01	3.83E-03	4.23E-08	7.87E-10
		TS4		
$\mathcal{E}_1$	2.14E-01	3.95E-03	5.99E-08	4.06E-12
$\mathcal{E}_0$	1.53E-01	2.94E-03	3.35E-08	3.88E-12
$\mathcal{E}_{-1}$	2.10E-01	3.83E-03	6.14E-08	3.67E-12

Table 2: Temporal discretization errors at time $t=0.4$ in Example 4.1.

τ	1/40	1/80	1/160	1/320	1/640
			TS2		
$\mathcal{E}_1$	4.94E-03	1.21E-03	3.03E-04	7.59E-05	1.89E-05
rate		2.01	2.00	2.00	2.00
$\mathcal{E}_0$	3.00E-03	7.43E-04	1.85E-04	4.63E-05	1.15E-05
rate		2.00	2.00	1.99	2.00
$\mathcal{E}_{-1}$	4.94E-03	1.21E-03	3.03E-04	7.59E-05	1.89E-05
rate		2.01	2.00	2.00	2.00
			TS4		
$\mathcal{E}_1$	6.22E-04	4.09E-05	2.59E-06	1.63E-07	1.02E-08
rate		3.92	3.97	3.99	3.99
$\mathcal{E}_0$	3.78E-04	2.56E-05	1.63E-06	1.03E-07	6.45E-09
rate		3.88	3.99	3.99	3.99
$\mathcal{E}_{-1}$	6.22E-04	4.09E-05	2.59E-06	1.63E-07	1.02E-08
rate		3.92	3.97	3.99	3.99

Example 4.2. To study the efficiency of **TS2** and **TS4**, let $d=2$, $\mathcal{D}=[-8,8]^2$, $\tau=10^{-3}$, $V=\frac{1}{2}(x^2+y^2)$, $c_0=100$, $c_1=2$ and $\gamma=1.2$. The initial data is chosen as

$$\psi_1^0=\psi_0^0=\psi_{-1}^0=\frac{1}{\sqrt{6\pi}}\phi(\mathbf{x}), \tag{4.3}$$

with $\phi(\mathbf{x})=e^{-(x^2+y^2)/2}$. Then we observe the computational time at $t=1$ by **TS2** and **TS4** for $N=64/128/256/512$, respectively.

Table 3: The CPU times (units of ω_m^{-1}) of **TS2** and **TS4** in Example 4.2.

N^2	**TS2**	**TS4**
64^2	1.53	3.52
128^2	6.71	14.74
256^2	29.52	66.33
512^2	135.66	297.36

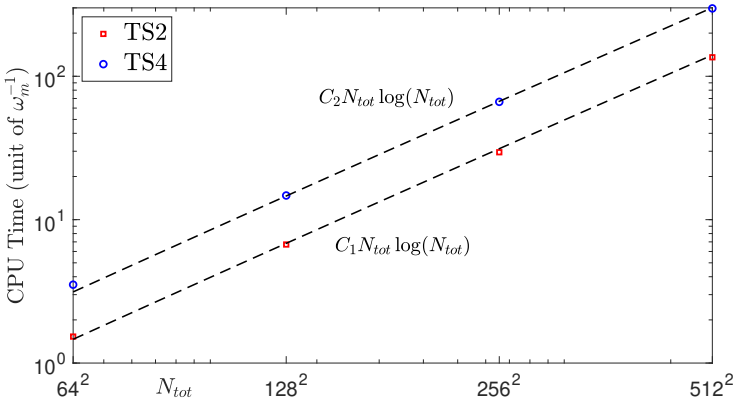

Figure 1: Log-log plot of timing results for TS2 and TS4 versus the total grid number N_{tot} in Example 4.2.

Table 3 and Fig. 1 present the computational time from $t=0$ to $t=1$ with time step $\tau=10^{-3}$ by **TS2** and **TS4** under different total grid number $N_{tot}:=N^2$. It shows that both the **TS2** and **TS4** are efficient and the CPU time scales roughly as $CN_{tot}\log(N_{tot})$, which achieves almost the optimal efficiency.

4.2 Dynamical laws verification

In this subsection, we study the dynamical properties, including the energy/mass/magnetization conservation and evolution of condensate widths. Hereafter, we take $\phi(\mathbf{x})=e^{-(x^2+y^2)/2}$, $\mathcal{D}=[-12,12]^2$, the mesh size $h=1/16$, time step size $\tau=10^{-3}$, and two different types of interactions are considered:

- **Case I.** With ferromagnetic interaction, e.g., $^{87}R_b$ confined in a cigar-shaped trapping potential with parameters: $m=1.443\times10^{-25}[kg]$, $a_0=5.387[nm]$, $a_2=5.313[nm]$, $\omega_x=\omega_y=2\pi\times20[Hz]$ and $\omega_z=2\pi\times400[Hz]$. This suggests to use dimensionless quantities in (1.4) for our computations as: $d=2$, $V(\mathbf{x})=\frac{1}{2}(x^2+y^2)$, $c_0\approx0.0885N$, and $c_1\approx-0.00041N$, with N the total number of atoms in the condensate and the dimensionless length unit $a_s=2.4116\times10^{-6}[m]$ and time unit $t_s=0.007958[s]$.

- **Case II.** With antiferromagnetic interaction, e.g., $^{23}N_a$ confined in a cigar-shaped trapping potential with parameters: $m=3.816\times10^{-26}[kg]$, $a_0=2.646[nm]$, $a_2=2.911[nm]$, $\omega_x=\omega_y=2\pi\times20[Hz]$ and $\omega_z=2\pi\times400[Hz]$. This suggests to us to use dimensionless quantities in (1.4) for our computations as: $d=2$, $V(\mathbf{x})=\frac{1}{2}(x^2+y^2)$, $c_0\approx0.0241N$, and $c_1\approx0.00075N$, with the dimensionless length unit $a_s=4.6896\times10^{-6}[m]$ and time unit $t_s=0.007958[s]$.

In this section, we fix $N=10^3$, and consider the following five types of initial data

$$(a)\ \ \psi_1^0=\psi_0^0=\psi_{-1}^0=\frac{1}{\sqrt{6\pi}}\phi(\mathbf{x}), \tag{4.4a}$$

$$(b)\ \ \psi_1^0=\psi_{-1}^0=\frac{1}{\sqrt{6\pi}}\phi(\mathbf{x}),\ \psi_0^0=\frac{i}{\sqrt{6\pi}}\phi(\mathbf{x}), \tag{4.4b}$$

$$(c)\ \ \psi_1^0=\psi_0^0=\frac{1}{\sqrt{6\pi}}\phi(\mathbf{x}),\ \psi_{-1}^0=\frac{1}{\sqrt{3\pi}}\phi(\mathbf{x}), \tag{4.4c}$$

$$(d)\ \ \psi_1^0=\psi_{-1}^0=\phi(\mathbf{x}),\ \psi_0^0=(x+iy)\phi(\mathbf{x}). \tag{4.4d}$$

$$(e)\ \ \psi_\ell^0=\psi_\ell^g(\mathbf{x}),\ \text{with}\ \Phi^g(\mathbf{x})=\left(\phi_1^g(\mathbf{x}),\phi_0^g(\mathbf{x}),\phi_{-1}^g(\mathbf{x})\right)^T\ \text{the ground state of (1.4).} \tag{4.4e}$$

Actually, the three component functions $\psi_\ell^0(\mathbf{x})$ $(\ell=1,0,-1)$ of the type (a) initial data are the same. The type (b) and type (c) initial data possess two equal component functions $\psi_1^0(\mathbf{x})=\psi_{-1}^0(\mathbf{x})$ and $\psi_1^0(\mathbf{x})=\psi_0^0(\mathbf{x})$, respectively. The component function $\psi_0^0(\mathbf{x})$ of the type (d) initial data has a vortex, whereas the type (e) initial data, i.e., the ground state of the corresponding SOC spin-1 BEC model, always leads to a soliton-type evolution. During the following examples, we take the SOC strength parameter $\gamma=0$, 1,3, which mean zero, medium and strong SOC strength, respectively. In fact, both the ground sates of **Case I** and **Case II** with $\gamma=1$ have stripe patterns, while the ground sates of **Case I** with $\gamma=3$ possess square-lattice patterns.

Example 4.3. (Mass and energy). To observe the evolutions of total/component mass and total energy, we simulate the dynamics of the SOC spin-1 BEC (1.4) for **Case I** (ferromagnetic) and **Case II** (antiferromagnetic) with the SOC strength $\gamma=1$ and the type (a) initial data, respectively.

Fig. 2 shows the evolution of total mass and component masses for **Case I** (ferromagnetic) and **Case II** (antiferromagnetic) with the SOC strength $\gamma=1$ and the type (a) initial data in Example 4.3, respectively. Fig. 3 shows the evolution of total energy for **Case I** and **Case II** in Example 4.3 by presenting $\frac{\mathcal{E}(t)}{\mathcal{E}_0(t)}-1$ (left) and $\mathcal{E}_{n+1}(t)-\mathcal{E}_n(t)$ (right). The numerical results illustrate that the total mass of the SOC spin-1 BEC is conserved while its component masses do not necessarily conserve. Meanwhile, the total energy is approximately conserved with high accuracy at the discrete level, since our method possesses second or fourth order accuracy in time direction. These results are consistent with our previous theoretical analysis.

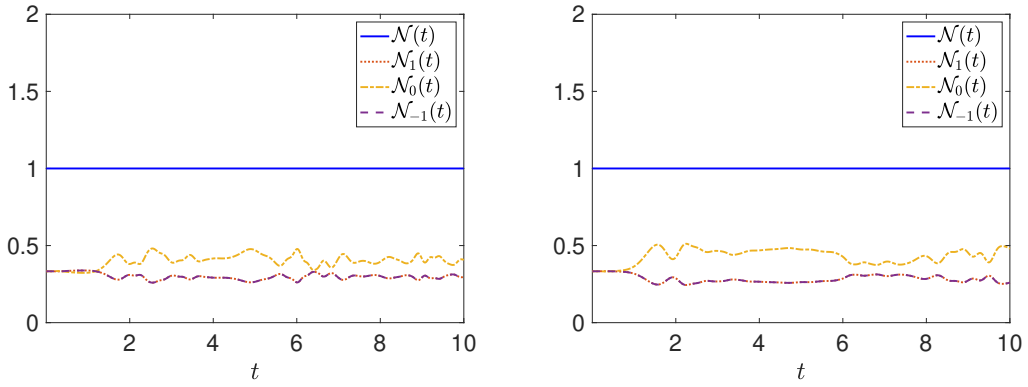

Figure 2: The evolution of total mass $\mathcal{N}(t)$ and component masses $\mathcal{N}_\ell(t)$ $(\ell=1,0,-1)$ with $\gamma=1$ for **Case I** (left) and **Case II** (right) in Example 4.3.

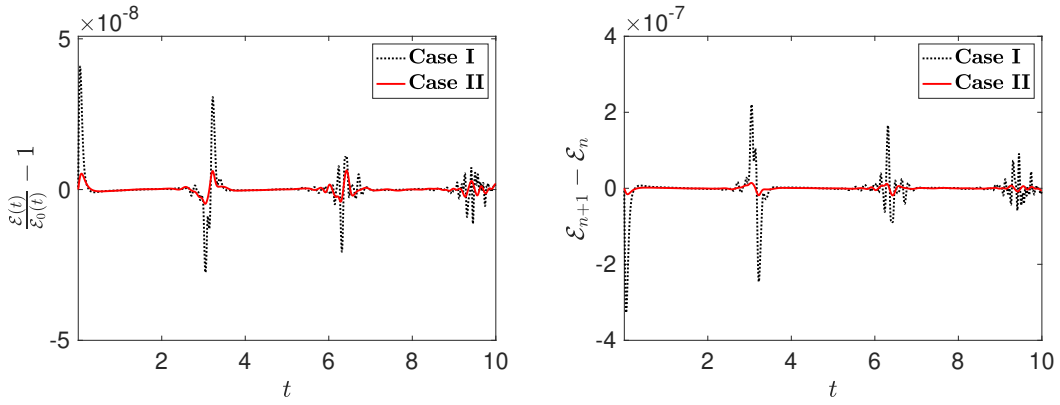

Figure 3: The evolution of $\frac{\mathcal{E}(t)}{\mathcal{E}_0(t)}-1$ (left) and $\mathcal{E}_{n+1}(t)-\mathcal{E}_n(t)$ (right) with $\gamma=1$ for **Case I** and **Case II** in Example 4.3.

Example 4.4. (magnetization). To observe the evolutions of total magnetization, we simulate the dynamics of the SOC spin-1 BEC (1.4) for **Case I** (ferromagnetic) and **Case II** (antiferromagnetic) with the SOC strength $\gamma=0$, 1 and initial data as type (a)-(c), respectively.

Figs. 4-5 present the evolution of total magnetization under different SOC strength and initial data in Examples 4.4. The numerical results tell that when $\gamma=0$, the total magnetizations conserve for both **Case I** and **Case II**, despite different initial data. These results are consistent with our previous theoretical results. However, when $\gamma\neq 0$, whether the total magnetization conserves depends on different initial data. Actually, one finds that the total magnetizations are conserved for the initial data such that $\psi_1^0(\mathbf{x})=\psi_{-1}^0(\mathbf{x})$. These observations are still open to be verified.

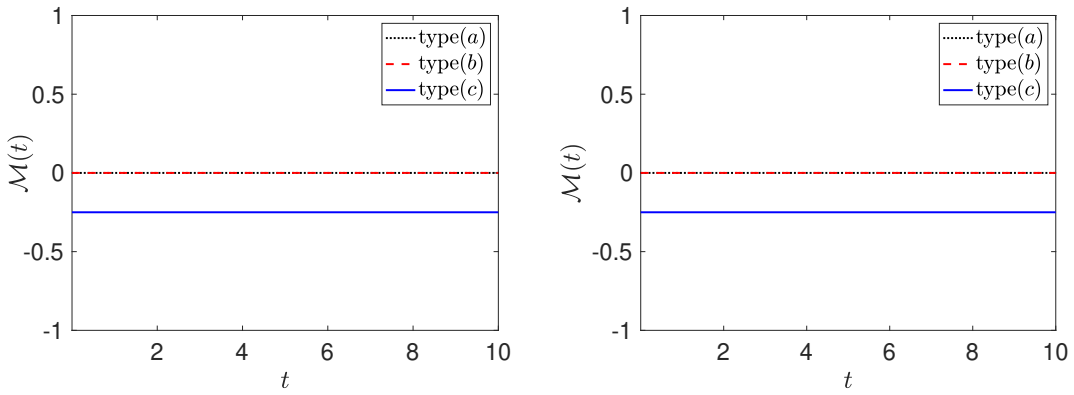

Figure 4: Dynamics of $\mathcal{M}(t)$ with $\gamma=0$ for **Case I** (left) and **Case II** (right) in Example 4.4.

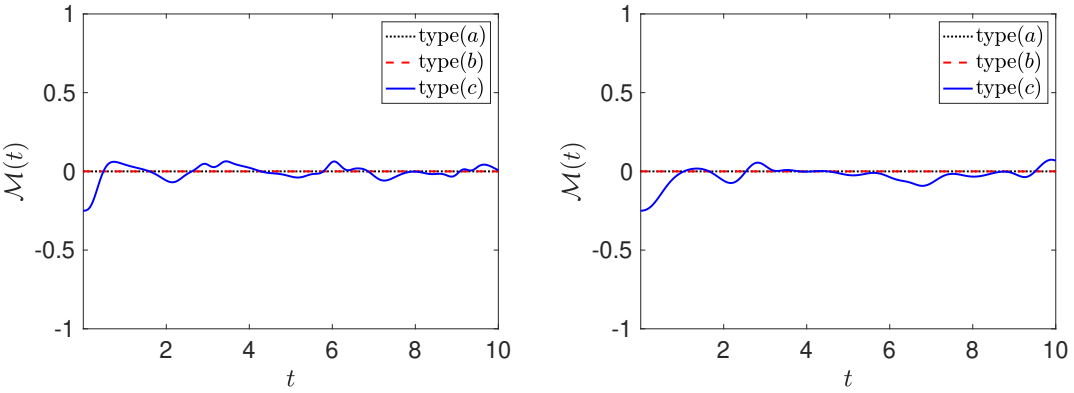

Figure 5: Dynamics of $\mathcal{M}(t)$ with $\gamma=1$ for **Case I** (left) and **Case II** (right) in Example 4.4.

Example 4.5. (condensate width). To observe the evolutions of condensate widths, we fix initial data as type (a), then simulate the dynamics of the SOC spin-1 BEC (1.4) for **Case I** (ferromagnetic) and **Case II** (antiferromagnetic) with the SOC strength $\gamma=0$, 3, respectively.

Figs. 6-7 show the evolution of the condensate widths with time when γ takes different values in Example 4.5. The experimental results confirm the results of theoretical analysis: for both **Case I** (ferromagnetic) and **Case II** (antiferromagnetic), when $\gamma=0$, the condensate width evolutions periodically with $\delta_x=\delta_y=\frac{1}{2}\delta_r$, and when $\gamma\neq0$, the evolution does not show periodicity.

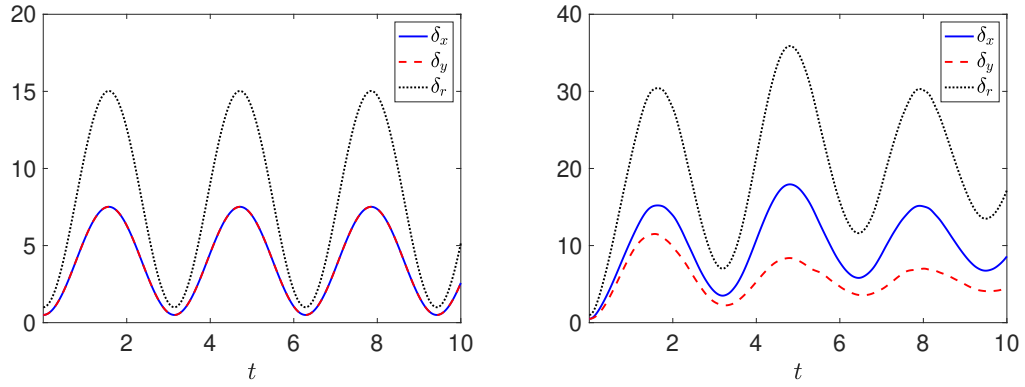

Figure 6: Dynamics of the condensate widths with $\gamma=0$ (left) and $\gamma=3$ (right) in **Case I** of Example 4.5.

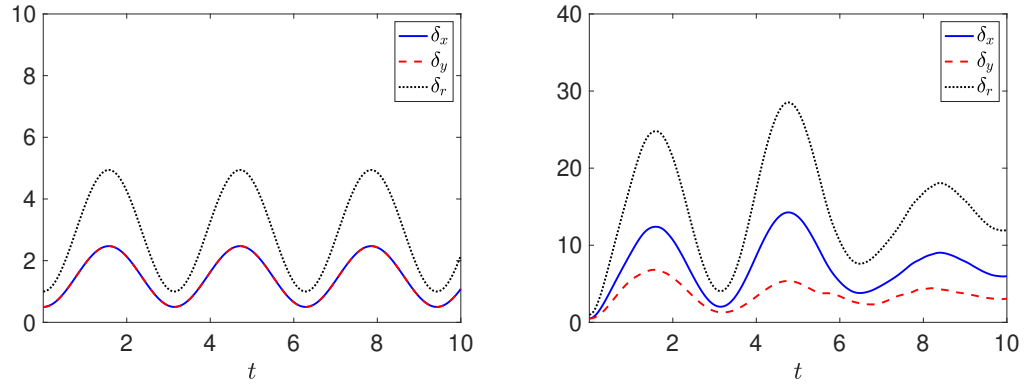

Figure 7: Dynamics of the condensate widths with $\gamma=0$ (left) and $\gamma=3$ (right) in **Case II** of Example 4.5.

4.3 Evolution of wave functions

In this subsection, we study the dynamics of wave functions under different SOC strength and initial data.

Example 4.6. To observe the evolutions of wave functions with different initial data, we fix the SOC strength $\gamma=3$, then simulate the dynamics of the SOC spin-1 BEC (1.4) for **Case I** (ferromagnetic) and **Case II** (antiferromagnetic) with the type (d) and (e) initial data, respectively.

Fig. 8 and Fig. 9 show the evolution of component density functions for **Case I** (ferromagnetic) and **Case II** (antiferromagnetic) with the initial data chosen as the corresponding ground sates, respectively. It is observed that both the square-lattice pattern of the ground state solution for the ferromagnetic case and the stripe-pattern of the ground state solution for the antiferromagnetic case are not changed during the evolution. Moreover,

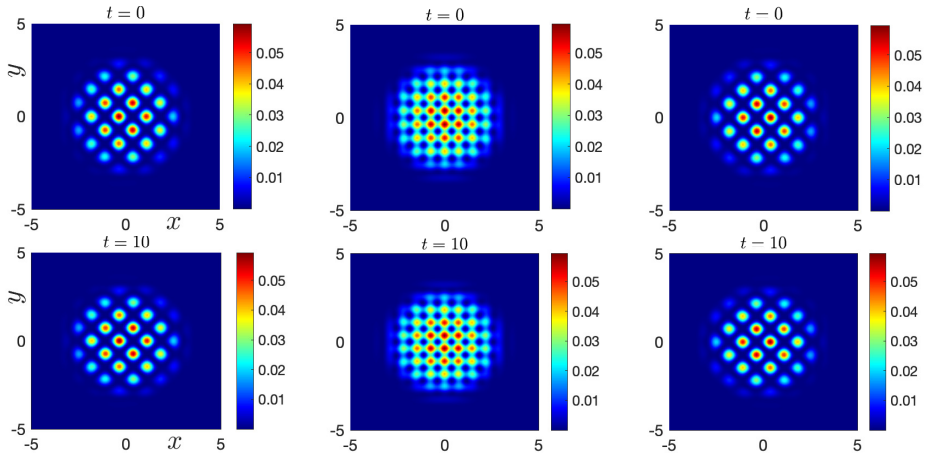

Figure 8: Contour plots of the density $|\psi_1|^2$, $|\psi_0|^2$ and $|\psi_{-1}|^2$ (from left column to right column) for **Case I** with the type (e) initial data in Example 4.6.

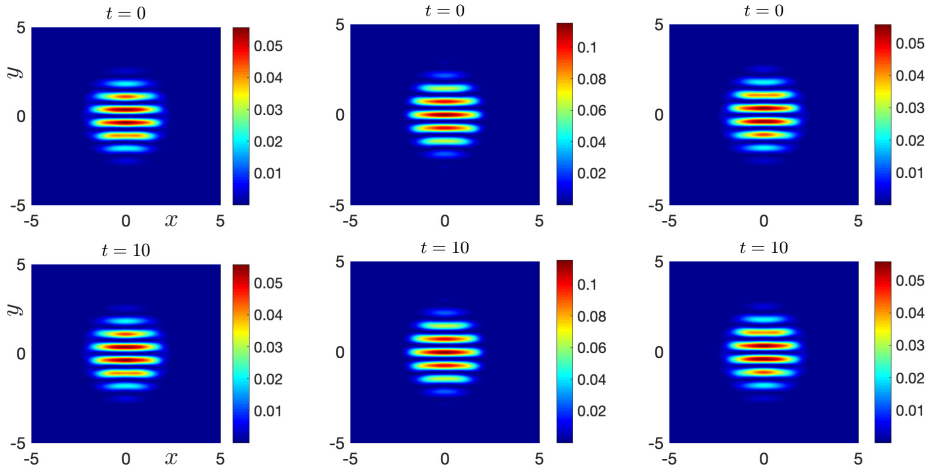

Figure 9: Contour plots of the density $|\psi_1|^2$, $|\psi_0|^2$ and $|\psi_{-1}|^2$ (from left column to right column) for **Case II** with the type (e) initial data in Example 4.6.

the numerical results illustrate that the evolutions of SOC spin-1 BECs possess the solitary wave properties if the initial data is chosen as ground states. Fig. 10 presents the dynamics of the SOC spin-1 BEC (1.4) for **Case I** and **Case II** with an initial data where $\psi_0^0(\mathbf{x})$ has a vortex. It is observed that during the evolution, the vortex of the initial data disappears and the condensate extends outwards with new patterns of the wave functions being generated.

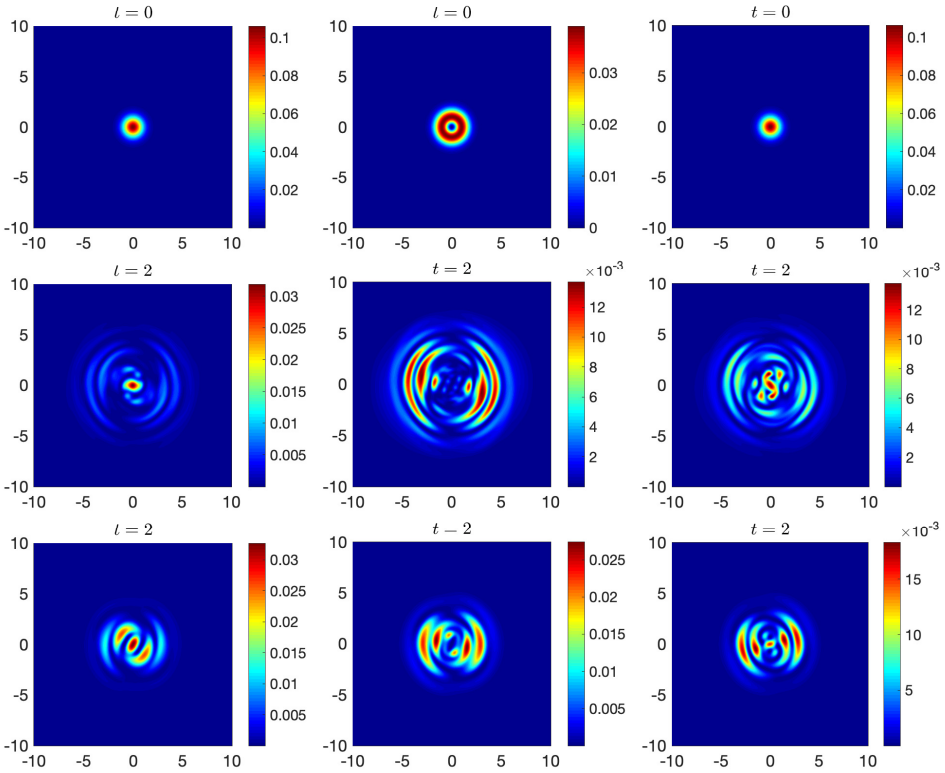

Figure 10: Contour plots of the density $|\psi_1|^2$, $|\psi_0|^2$ and $|\psi_{-1}|^2$ (from left column to right column) for the type (d) initial data (the upper row), and the wave functions of **Case I** (the middle row) and **Case II** (the bottom row) at $t=2$ in Example 4.6.

Example 4.7. To observe the evolutions of wave functions with different SOC strength, we fix initial data as type (a), then simulate the dynamics of the SOC spin-1 BEC (1.4) for **Case I** and **Case II** with the SOC strength $\gamma=0$, 1, 3, respectively.

Fig. 11 and Fig. 12 show the evolution of component density functions at $t=2$ for **Case I** (ferromagnetic) and **Case II** (antiferromagnetic) with different SOC strength. It is observed that: (1) for both cases, the wave functions of the condensates are no longer evolved as solitary waves, since the initial data are not taken as the stationary state of the SOC spin-1 BEC (1.4). However, when $\gamma=0$, the gaussian type pattern of the type (a) initial data are not changed during the evolution, with the condensates extending outwards. (2) when $\gamma\neq 0$, for both cases the gaussian type pattern of the initial data changes continuously and new patterns of the wave functions will be generated during the evolution. (3) when the SOC strength γ turns larger, the condensate extends outwards more quickly and the component wave functions possess more wavelets.

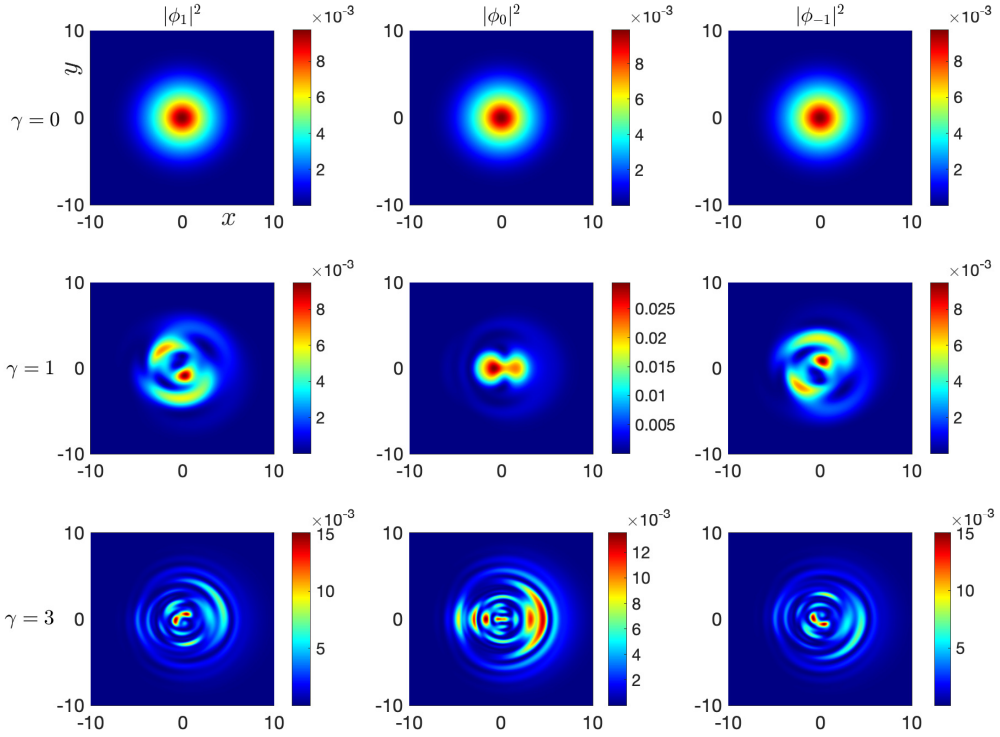

Figure 11: Contour plots of the density $|\psi_1|^2$, $|\psi_0|^2$ and $|\psi_{-1}|^2$ (from left column to right column) at $t=2$ in Example 4.7 for **Case I** with $\gamma=0$, 1 and 3 (from upper row to bottom row), respectively.

5 Conclusions

We proposed an efficient two-step time splitting Fourier spectral method to simulate the dynamics of SOC spin-1 BECs. The Hamiltonian was split into the linear part, including the Laplace and SOC terms, and the nonlinear part (the remaining terms). The linear and nonlinear subproblems were integrated exactly and explicitly in phase space and physical space, respectively. Based on such two-step splitting, we constructed the second and fourth order schemes to simulate the dynamics, noticing that higher-order schemes can also be easily constructed if necessary. Our method is spectrally accurate in space and high order in time, and it is explicit and unconditionally stable. The dynamical laws of total mass, energy, magnetization and condensate widths were derived and confirmed numerically. The accuracy and efficiency of our method were also verified by extensive numerical results. Moreover, the method proposed can be readily generalized to simulate spin-F BECs and other related models, such as the SOC (droplet) dipolar BEC.

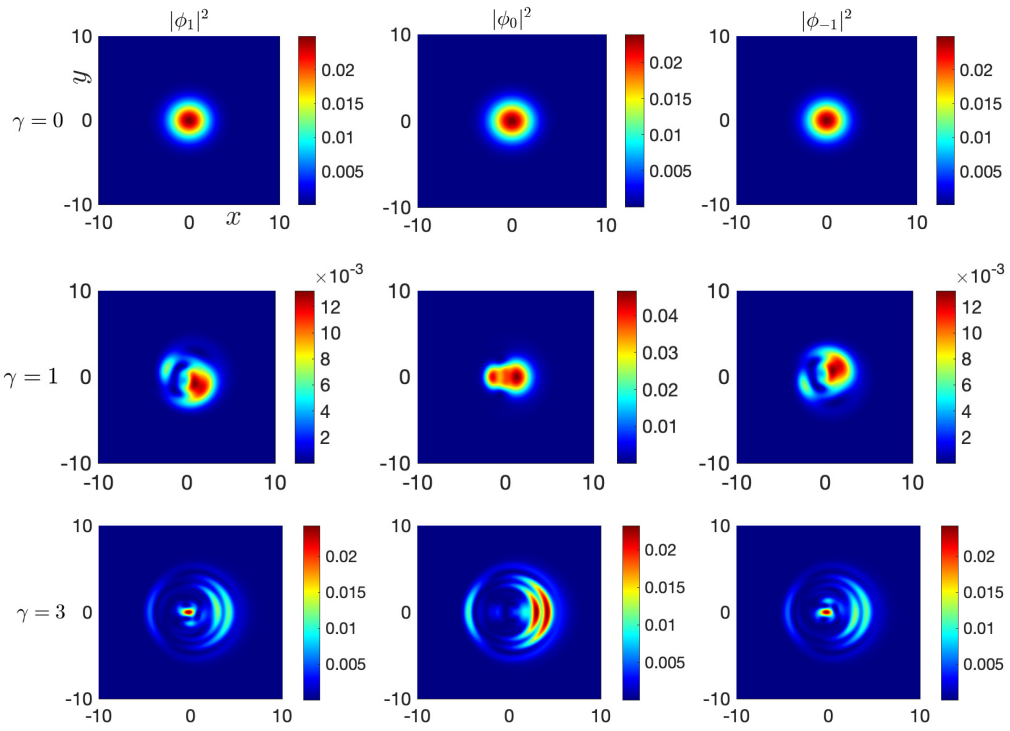

Figure 12: Contour plots of the density $|\psi_1|^2$, $|\psi_0|^2$ and $|\psi_{-1}|^2$ (from left column to right column) at $t=2$ in Example 4.7 for **Case II** with $\gamma=0$, 1 and 3 (from upper row to bottom row), respectively.

Acknowledgments

This work was partially supported by the National Key R&D Program of China (No. 2024YFA1012803) (Y. Zhang), the basic research fund of Tianjin University (No. 2025XJ21-0010) (Y. Zhang), and the National Natural Science Foundation of China Nos. 12471375, 11971007 (Y. Yuan) and No. 12271400 (Y. Zhang).

References

[1] M. H. Anderson, J. R. Ensher, M. R. Matthews, C. E. Wieman and E. A. Cornell, Observation of Bose-Einstein condensation in a dilute atomic vapor, *Science*, 269(5221) (1995), 198-201.

[2] P. Banger, P. Kaur, Arko Roy and S. Gautam, FORTRESS: FORTRAN programs to solve coupled Gross-Pitaevskii equations for spin-orbit coupled spin-f Bose-Einstein condensate with spin $f=1$ or 2, *Comp. Phys. Comm.*, 279 (2022), 108442.

[3] W. Bao and Y. Cai, Mathematical models and numerical methods for spinor Bose-Einstein condensates, *Commun. Comput. Phys.*, 24 (2018), 899-965.

[4] W. Bao and Y. Cai, Mathematical theory and numerical methods for Bose-Einstein condensation, *Kinet. Relat. Models*, 6 (2013), 1-135.
[5] W. Bao, D. Jaksch and P. Markowich, Numerical solution of the Gross-Pitaevskii equation for Bose-Einstein condensation, *J. Comput. Phys.*, 187(1) (2003), 318-342.
[6] W. Bao, D. Marahrens, Q. Tang and Y. Zhang, A simple and efficient numerical method for computing the dynamics of rotating Bose-Einstein condensates via rotating Lagrangian coordinates, *SIAM J. Sci. Comput.*, 35 (2013), A2671-A2695.
[7] W. Bao and J. Shen, A fourth-order time-splitting Laguerre-Hermite pseudospectral method for Bose-Einstein condensates *SIAM J. Sci. Comput.*, 26(6) (2005), 2010-2028.
[8] W. Bao and H. Wang, An efficient and spectrally accurate numerical method for computing dynamics of rotating Bose-Einstein condensates, *J. Comput. Phys.*, 217 (2006), 612-626.
[9] W. Bao and Y. Zhang, Dynamical laws of the coupled Gross-Pitaevskii equations for spin-1 Bose-Einstein condensates, *Methods Appl. Anal.*, 17 (2010), 49-80.
[10] Y. Cai and W. Liu, Efficient and accurate gradient flow methods for computing ground states of spinor Bose-Einstein condensates, *J. Comput. Phys.*, 433 (2021), 110183.
[11] K. B. Davis, M. O. Mewes, M. R. Andrews, N. J. van Druten, D. S. Durfee, D. M. Kurn and W. Ketterle, Bose-Einstein condensation in a gas of sodium atoms, *Phys. Rev. Lett.*, 75 (1995), 3969-3973.
[12] B. Fornberg and T. A. Driscoll, A fast spectral algorithm for nonlinear wave equations with linear dispersion, *J. Comput. Phys.*, 155(2) (1999), 456-467.
[13] K. Gawryluk, T. Karpiuk, M. Gajda, K. Rzazewski and M. Brewczyk, Unified way for computing dynamics of Bose-Einstein condensates and degenerate Fermi gases, *Int. J. Comput. Math.*, 95(11) (2018), 2143–2161.
[14] M. Z. Hasan and C. L. Kane, Colloquium: Topological insulators, *Rev. Mod. Phys.*, 82 (2010), 3045-3067.
[15] Y. K. Kato, R. C. Myers, A. C. Gossard and D. D. Awschalom, Observatioin of the spin Hall effect in semiconductors, *Science*, 306 (2004), 1910-1913.
[16] P. Kaur, Arko Roy and S. Gautam, FORTRESS: FORTRAN programs for solving coupled Gross-Pitaevskii equations for spin-orbit coupled spin-1 Bose-Einstein condensate, *Comp. Phys. Comm.*, 259 (2021), 107671.
[17] Y. Kawaguchi and M. Ueda, Spinor Bose-Einstein condensates, *Physics Reports*, 520(5) (2012), 253-381.
[18] J. D. Koralek, C. P. Weber, J. Orenstein, B. A. Bernevig, S. C. Zhang, S. Mack and D. D. Awschalom, Emergence of the persistent spin helix in semiconductor quantum wells, *Nature*, 458 (2009), 610-613.
[19] R. Liao, Y. X. Yu and W. M. Liu, Tuning the tricritical point with spin-orbit coupling in polarized Fermionic condensates, *Phys. Rev. Lett.*, 108 (2012), 080406.
[20] Y. J. Lin, R. L. Compton, K. Jiméz-Garcia, J. V. Porto and I. B. Spielman, Synthetic magnetic fields for ultracold neutral atoms, *Nature*, 462 (2009), 628-632.
[21] Y. J. Lin, R. L. Compton, A. R. Perry, W. D. Phillips, J. V. Porto and I. B. Spielman, Bose-Einstein condensates in a uniform light-induced vector potential, *Phys. Rev. Lett.*, 102 (2009), 130401.
[22] Y. J. Lin, K. Jiménez-Garcia and I. B. Spielman, Spin-orbit-coupled Bose-Einstein condensates, *Nature*, 471(7336) (2011), 83-86.
[23] L. M. Symes, R. I. McLachlan and P. B. Blakie, Efficient and accurate methods for solving the time-dependent spin-1 Gross-Pitaevskii equation, *Phys. Rev. E*, 93(5) (2016), 053309.
[24] L. M. Symes and P. B. Blakie, Solving the spin-2 Gross-Pitaevskii equation using exact non-

linear dynamics and symplectic composition, *Phys. Rev. E*, 95(1-1) (2017), 013331.
[25] H. Wang, A time-splitting spectral method for computing dynamics of spinor F = 1 Bose-Einstein condensates, *Int. J. Comput. Math.*, 84 (2007), 925-944.
[26] H. Wang, An efficient numerical method for computing dynamics of spin F = 2 Bose-Einstein condensates, *J. Comput. Phys.*, 230(15) (2011), 6155-6168.
[27] F. Wilczek, Majorana returns, *Nat. Phys.*, 5 (2009), 614-618.
[28] H. Yoshida, Construction of higher order symplectic integrators, *Phys. Rev. A*, 150(5-7) (1990), 262-268.
[29] Y. Yuan, Z. Xu, Q. Tang and H. Wang, The numerical study of the ground states of spin-1 Bose-Einstein condensates with spin-orbit-coupling, *E. Asian J. Appl. Math.*, 8 (2018), 598-610.
[30] C. Zhang, Spin-orbit coupling and perpendicular zeeman field for fermionic cold atoms: Observation of the intrinsic anomalous hall effect, *Phys. Rev. A*, 82(2) (2010), 021607.
[31] X. Zhang, B. Li and S. Zhang, Rotating spin-orbit coupled Bose-Einstein condensates in concentrically coupled annular traps, *Laser Phys.*, 23 (2013), 105501.